



Cite this: DOI: 10.1039/c5nr03119b

A challenge for theranostics: is the optimal particle for therapy also optimal for diagnostics?†

Tamar Dreifuss,^a Oshra Betzer,^{a,b} Malka Shilo,^a Aron Popovtzer,^c Menachem Motiei^a and Rachela Popovtzer*^a

Theranostics is defined as the combination of therapeutic and diagnostic capabilities in the same agent. Nanotechnology is emerging as an efficient platform for theranostics, since nanoparticle-based contrast agents are powerful tools for enhancing *in vivo* imaging, while therapeutic nanoparticles may overcome several limitations of conventional drug delivery systems. Theranostic nanoparticles have drawn particular interest in cancer treatment, as they offer significant advantages over both common imaging contrast agents and chemotherapeutic drugs. However, the development of platforms for theranostic applications raises critical questions; is the optimal particle for therapy also the optimal particle for diagnostics? Are the specific characteristics needed to optimize diagnostic imaging parallel to those required for treatment applications? This issue is examined in the present study, by investigating the effect of the gold nanoparticle (GNP) size on tumor uptake and tumor imaging. A series of anti-epidermal growth factor receptor conjugated GNPs of different sizes (diameter range: 20–120 nm) was synthesized, and then their uptake by human squamous cell carcinoma head and neck cancer cells, *in vitro* and *in vivo*, as well as their tumor visualization capabilities were evaluated using CT. The results showed that the size of the nanoparticle plays an instrumental role in determining its potential activity *in vivo*. Interestingly, we found that although the highest tumor uptake was obtained with 20 nm C225-GNPs, the highest contrast enhancement in the tumor was obtained with 50 nm C225-GNPs, thus leading to the conclusion that the optimal particle size for drug delivery is not necessarily optimal for imaging. These findings stress the importance of the investigation and design of optimal nanoparticles for theranostic applications.

Received 12th May 2015,
Accepted 3rd August 2015
DOI: 10.1039/c5nr03119b

www.rsc.org/nanoscale

Introduction

The concept of “theranostics” was first proposed in 2000 by Harrell and Kopelman,¹ and coined by Funkhouser in 2002.² Theranostics is defined as a combination of therapeutic and diagnostic imaging capabilities in a single agent. Recent advances in nanotechnology have provided an efficient platform for theranostics. Nanoparticle-based contrast agents offer improved capabilities for specific targeting, high-resolution imaging and prolonged circulation times in comparison with the commonly used contrast compounds.³ In addition, therapeutic nanoparticles can overcome various limitations of conventional drug delivery systems, such as nonspecific targeting, lack of water solubility, poor oral bioavailability, and low thera-

peutic indices.^{4,5} Co-delivery of these imaging and therapeutic functions by specifically tailored theranostic nanosystems can considerably enhance personalized medicine.⁶

Theranostic nanoparticles have drawn particular interest in cancer treatment, as they offer significant advantages over both common imaging contrast agents and chemotherapeutic drugs. The leaky nature of the tumor vasculature allows nanoparticles to accumulate selectively at the tumor site *via* a passive targeting pathway, referred to as the enhanced permeability and retention (EPR) effect.^{7,8} Furthermore, the high surface-area-to-volume ratio that characterizes nano-sized materials enables high loading, which can be exploited to actively target nanoparticles to the tumor and to deliver high doses of the therapeutic agent to the diseased tumor tissue. Indeed, numerous theranostic nanoplatfoms have been investigated for cancer treatment,⁹ including magnetic nanoparticles,^{10,11} carbon nanotubes,¹² gold nanomaterials,^{13–15} polymeric nanoparticles^{16,17} and silica nanoparticles.¹⁸

Clinically used diagnostic modalities, including computed tomography (CT), magnetic resonance imaging (MRI) and ultrasound (US) analysis, provide anatomical information based on endogenous contrast. Although nanoparticle-based

^aFaculty of Engineering and the Institutes of Nanotechnology & Advanced Materials, Bar-Ilan University, Ramat-Gan, Israel. E-mail: rachela.popovtzer@biu.ac.il

^bGonda Brain Research Center, Bar-Ilan University, Ramat-Gan, Israel

^cDavidoff cancer center, Rabin Medical Center, Beilinson Campus, Petah Tiqwa, Israel

†Electronic supplementary information (ESI) available. See DOI: 10.1039/c5nr03119b

contrast agents can enhance *in vivo* imaging,^{3,19–21} the effect of different nanoparticle properties, including size, on the final tomographic image depends on the particular principles of each imaging modality. The size of the nanoparticle also has a significant impact on biological systems.²² Both *in vitro* and *in vivo* studies have demonstrated the dependence of cellular uptake,^{23,24} tissue biodistribution^{25–28} and tumor uptake^{29–32} on the nanoparticle size. Accordingly, designing nanoparticles for tumor imaging is often based on such reports, assuming the logical, but insufficiently supported premise, that maximum tumor uptake leads to maximum imaging capability.

This assumption has been examined here with a system that utilizes gold nanoparticles (GNPs) both as CT contrast agents and as a model system for drug delivery vehicles. GNPs are optimal contrast agents for CT, due to the relatively high X-ray attenuation of gold and the stability of gold colloids. Moreover, GNPs are easy to synthesize, and their size and shape can be precisely controlled. GNPs are also highly suitable for drug delivery systems, due to their strong binding affinity toward thiol, disulfide and amine groups, which enables binding with various targeting agents and therapeutic moieties. Several studies have presented the feasibility of GNPs as specific CT contrast agents for cancer imaging, including a recent study published by us which demonstrated that a small tumor, undetectable by anatomical CT, becomes clearly visible using molecularly targeted GNPs.³³ However, when developing such theranostic nanoplatforms, critical issues should be addressed, such as the effect of the particle's various chemical and physical parameters on diagnostic capabilities, and whether the optimal particle for diagnostics is also optimal for therapy.

In order to address these issues, an investigation of the effect of GNP size on tumor uptake and tumor visualization by CT was undertaken. For this aim, GNPs of various sizes (20 nm, 50 nm, 80 nm and 120 nm) were synthesized and coated with C225, an anti-epidermal growth factor receptor (EGFR) monoclonal antibody. The head and neck squamous cell carcinoma (SCC) was selected as a model system, since such tumors are associated with the EPR effect³⁴ and known to extremely overexpress EGFR.^{35,36} The anti-EGFR antibody is thus specific to head and neck SCC cells and therefore, the interaction between C225-GNPs and the tumor relies both on passive targeting (EPR effect) and active targeting (antibody–antigen interaction).³³ Tumor uptake and tumor visualization capabilities using CT were investigated for all GNP sizes. It was found that in this system, the optimal particle size for imaging was 50 nm, while the optimal size for maximum tumor uptake was 20 nm. In addition to the useful optimization that we present for this specific system, these results pose a challenge for designing optimal theranostic nanoparticles and thus, are important for future developments in this field.

Experimental

Gold nanosphere synthesis, conjugation and characterization

Synthesis. Synthesis of 20 nm spherical GNPs was carried out using sodium citrate as a reducing agent, based on

Enüstün & Turkevici's methodology.³⁷ 414 μL of 50% w/v HAuCl_4 solution were added to 200 mL purified water, and the solution was heated in an oil bath on a heating plate until boiling. Then, 4.04 mL of 10% sodium citrate solution were added, and the solution was stirred for 10 min. After cooling to room temperature, the solution was centrifuged until precipitation of the nanoparticles.

Synthesis of 50 nm, 80 nm and 120 nm GNPs was carried out by a growth process of 15 nm gold seeds, through addition of appropriate amounts of HAuCl_4 and MSA (2-mercaptosuccinic acid, Molekula) solutions to the seed solution. For seed creation, 10.4 μL of 50% w/v HAuCl_4 solution were diluted in 11 mL purified water. The solution was boiled on a heating plate and then 100 μL of 8.8% sodium citrate solution were added. After 5 min of stirring on a hot plate, the solution was cooled to room temperature and diluted to a total volume of 50 mL.

For 50 nm GNP synthesis, 6.5 mL of the seed solution and 88.4 μL of 50% w/v HAuCl_4 solution were added to 200 mL purified water. While stirring, 7.5 mL of 0.04 M MSA solution were added. The solution was stirred for 30 min and then centrifuged until precipitation of nanoparticles. The same procedure was followed for synthesis of 80 nm GNPs, with double amounts of HAuCl_4 and MSA solutions (176.8 μL of 50% w/v HAuCl_4 solution and 15 mL of 0.04 M MSA solution). For synthesis of 120 nm GNPs, the last procedure was followed, with addition of another three portions of 176.8 μL of 50% w/v of HAuCl_4 solution and 15 mL of 0.04 M MSA solution, every 30 min.

Conjugation. GNPs were coated with a PEG layer, in order to prolong nanoparticles' blood circulation time and to protect nanoparticles from detection by the immune system.^{38,39} The PEG layer consists of a mixture of thiol-polyethylene-glycol (mPEG-SH) ($\sim 85\%$, $M_w \sim 5$ kDa) and a heterofunctional thiol-PEG-acid (SH-PEG-COOH) ($\sim 15\%$, $M_w \sim 5$ kDa).⁴⁰ To each solution with the various GNP sizes, the PEG mixture was added in excess and the solutions were stirred for 4 h at room temperature. Following this step, the solutions were centrifuged in order to remove excess PEG molecules and reach higher concentrations. The C225 (Erbitux, Merck KGaA, Darmstadt, Germany) layer, which specifically targets the EGF receptor, was then covalently conjugated to the carboxylic group of the SH-PEG-COOH ($\sim 1 \times 10^2$, $\sim 10 \times 10^2$, $\sim 20 \times 10^2$ and $\sim 50 \times 10^2$ antibodies per nanoparticle, for 20 nm, 50 nm, 80 nm and 120 nm GNPs, respectively), after activation with EDC (1-ethyl-3-(3-dimethylaminopropyl) carbodiimide HCl, Thermo Scientific) and NHS (*N*-hydroxysulfosuccinimide sodium salt, Chem-Impex International),⁴⁰ by adding all three to the PEG-GNP solution and stirring the mixture overnight. Centrifugation was performed until a final Au concentration of 30 mg mL^{-1} was reached (Fig. 1 and 2).

Characterization. Transmission electron microscopy (TEM, JEM-1400, JEOL) was used to measure the size and shape of the GNPs, which were further characterized using dynamic light scattering (DLS), ultraviolet-visible spectroscopy (UV-Vis; UV-1650 PC; Shimadzu Corporation, Kyoto Japan), and zeta potential (ZetaSizer 3000HS; Malvern Instruments, Malvern, UK), following each level of coating.

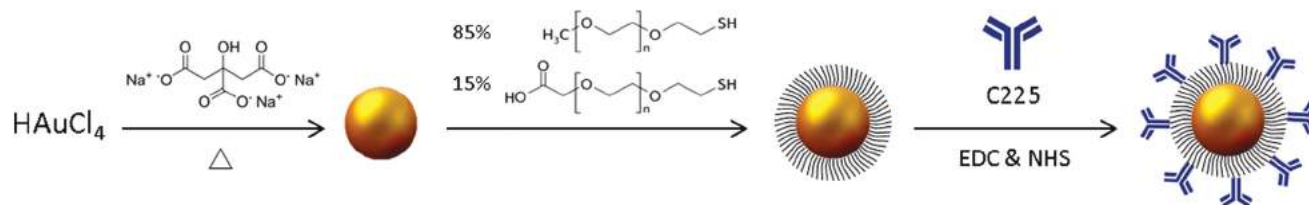


Fig. 1 Schematic diagram for the synthesis of 20 nm anti-EGFR-coated (C225) GNPs.

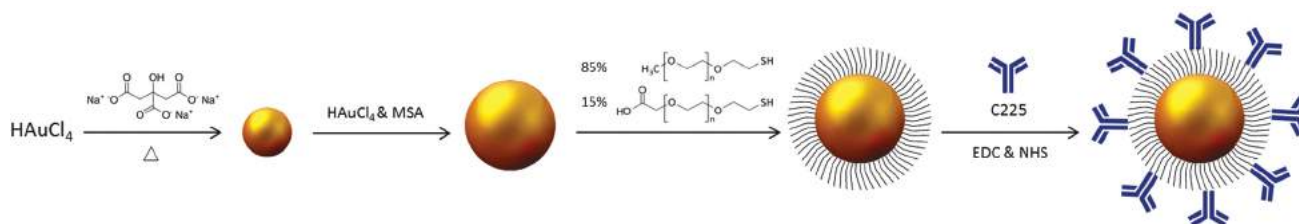


Fig. 2 Schematic diagram for the synthesis of 50 nm, 80 nm and 120 nm anti-EGFR-coated (C225) GNPs.

In vitro cell binding study

Human SCC A431 cells, which highly express EGFR on their cell surface, were seeded in 60 mm dishes (1×10^6 cells per dish), with 5 mL of Dulbecco's modified Eagle's medium (DMEM) containing 5% fetal calf serum, 0.5% penicillin, and 0.5% glutamine. Each of the four nanoparticle types were incubated with A431 cells (three samples for each type) at a final total concentration of $60 \mu\text{g mL}^{-1}$. A negative control experiment with 20 nm GNPs coated with anti-rabbit immunoglobulin G (IgG) antibody was conducted in order to demonstrate the functionality and specificity of the interaction. After 2 h incubation with the nanoparticles, the medium was removed and cells were washed three times with PBS to remove excess GNPs. Then, cells were collected and gold concentrations in the samples were measured using Flame Atomic Absorption Spectroscopy (FAAS). The number of GNPs within the cells was calculated according to the particle diameter.

Animal model and *in vivo* experiments

A431 cells (2×10^6) were injected subcutaneously into the back flank area of nude mice aged 6 weeks. When the tumor reached a diameter of 4–5 mm, the four different sized GNPs (30 mg mL^{-1}) were intravenously injected ($200 \mu\text{L}$, 300 mg per kg body weight) into their tail vein (3 mice for each GNP size). 24 h after injection, the mice were sacrificed and gold concentrations in the tumor and main organs (liver, spleen, kidneys and blood) were measured by FAAS. CT scans were performed before injection and at several time points, up to 24 h post-injection of GNPs. An additional 2 mice were used to further investigate the kinetics of 50 nm GNPs, up to 48 h post-injection. The study was conducted in compliance with the protocols approved by the Animal Care and Use Committees of Bar Ilan University, Ramat Gan, Israel.

FAAS analysis

Flame Atomic Absorption Spectroscopy (FAAS, SpectrAA 140, Agilent Technologies) was used to determine amounts of gold in the investigated samples. Cell samples from the *in vitro* experiments were dissolved in $100 \mu\text{L}$ aqua regia acid (a mixture of nitric acid and hydrochloric acid in a volume ratio of 1:3) and diluted with purified water to a total volume of 4 mL. Tissues taken in the *in vivo* experiment were melted with 1 mL aqua regia acid and then evaporated and diluted to a total volume of 10 mL. After filtration of the samples, gold concentrations were determined according to absorbance values, with correlation with calibration curves, constructed from solution with known gold concentrations.

Micro-CT scans

In vivo scans of the tumor regions were performed using a micro-CT scanner (Skyscan High Resolution Model 1176) with a nominal resolution of $35 \mu\text{m}$, a 0.2 mm aluminum filter, and a tube voltage of 45 kV. Reconstruction was done with a modified Feldkamp⁴¹ algorithm using the SkyScanNRecon software accelerated by GPU.⁴² Ring artifact reduction, Gaussian smoothing (3%), and beam hardening correction (20%) were applied. Volume rendered three-dimensional (3D) images were generated using an RGBA transfer function in SkyScan CT-Volume ("CTVol") software.

Results and discussion

Gold nanosphere synthesis, conjugation and characterization

Anti-EGFR-coated C225 GNPs (C225-GNPs) have been successfully synthesized in four different diameters: 20 nm, 50 nm, 80 nm and 120 nm, as observed by TEM analysis (Fig. 3). The hydrodynamic diameter before and after conjugation was

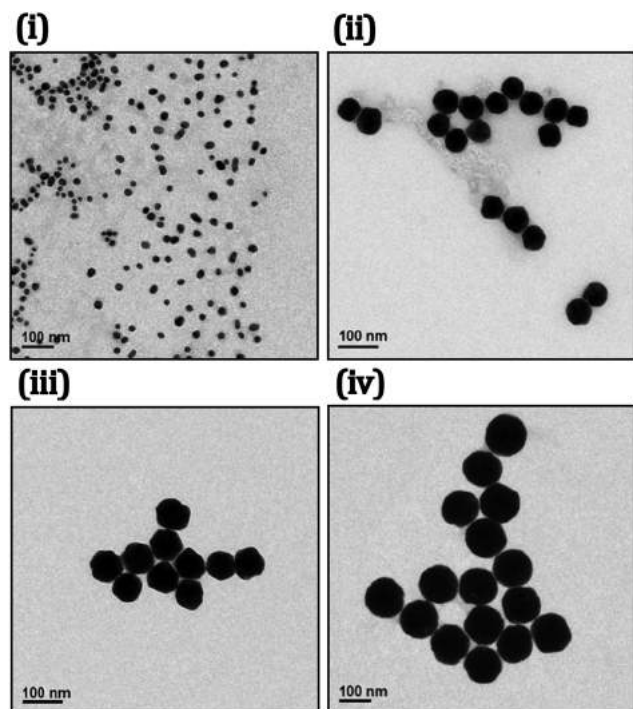


Fig. 3 TEM images of: (i) 20 nm, (ii) 50 nm, (iii) 80 nm and (iv) 120 nm GNPs (scale bar 100 nm).

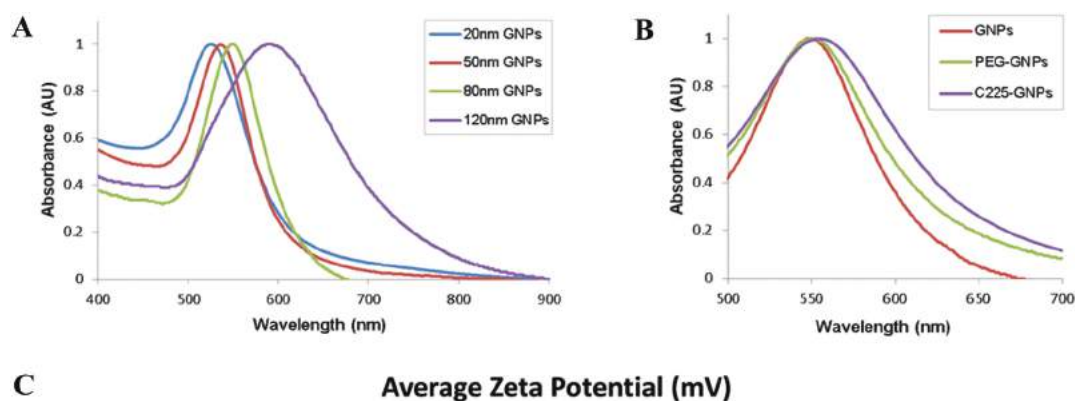
determined using DLS (ESI Table 1†). The UV-Vis spectrum of the GNPs also demonstrated size differences, while the surface plasmon resonance (SPR) peak ranged from 525 nm to

589 nm, according to the particle diameter (Fig. 4A). Conjugation of GNPs to the PEG layer as the first step, and to the anti-EGFR antibody as the second step, was confirmed by UV-Vis plasmon resonance shift and expansion and by zeta-potential measurements (Fig. 4B and C). The UV-vis spectra (Fig. 4B, ESI Fig. 1†) show a slight red shift in the particles following each step of conjugation, which is attributed to the change in the surrounding environment of the GNPs, as previously described in ref. 43 and 44.

In vitro cell binding study

The functionality of the interaction between the C225-GNPs and the A431 cells was previously published by us.³³ Briefly, control GNPs, coated with anti-rabbit IgG antibodies, were incubated with the A431 cells and their uptake was compared with the specifically targeted C225-GNPs. The uptake of the C225-GNPs was 10 times larger than the uptake of control IgG-GNPs,³³ demonstrating their specific interaction.

In order to investigate the effect of the nanoparticle size on its uptake probability by tumor cells, A431 SCC cells were incubated with the four types of C225-GNPs (20 nm, 50 nm, 80 nm and 120 nm) for 2 h, and atomic absorption spectroscopy was used to quantitatively determine the amount of internalized Au. The amount of gold was then translated to the number of GNPs per single cell, and to the total surface area per single cell. The results, as shown in Fig. 5, demonstrate significant dependence of cellular uptake on the particle size. Maximum uptake by cells, in terms of both total amount of gold and total surface area, was obtained with 120 nm C225-GNPs, while 20 nm C225-GNPs exhibited very poor uptake. However,



	20nm	50nm	80nm	120nm
Bare GNPs	-38.5±2.09	-40.26±0.45	-33.62±0.96	-30.60±0.72
PEG-GNPs	-21.23±0.60	-43.93±0.58	-40.33±0.59	-37.83±0.11
C225-GNPs	-25.23±0.15	-33.33±0.11	-31.13±0.21	-29.05±0.49

Fig. 4 Characterization of C225-GNPs: (A) ultraviolet-visible spectroscopy (UV-Vis) of 20 nm, 50 nm, 80 nm and 120 nm GNPs. Each size exhibits a peak at different wavelengths: 525 nm, 535 nm, 549 nm and 589 nm, respectively. (B) UV-Vis of bare GNPs, PEG-coated GNPs and final C225-GNPs, for 80 nm GNPs: the UV-Vis plasmon resonance shift and expansion indicate the different coating layers. (C) Zeta-potential measurements of bare GNPs, PEG-coated GNPs and final C225-GNPs, for all GNP sizes.

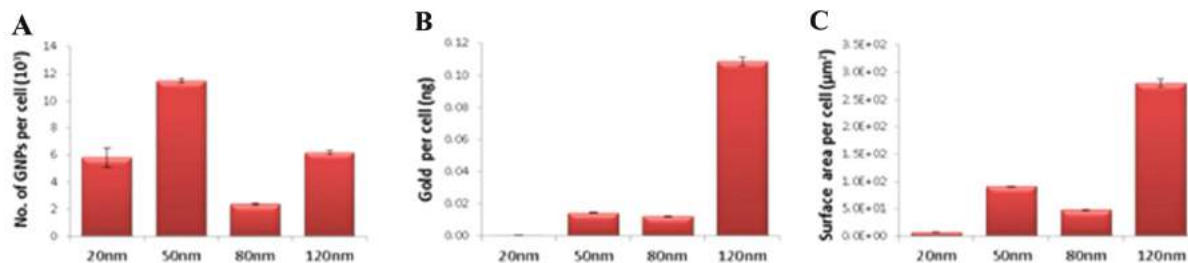


Fig. 5 Dependence of cellular uptake of spherical C225-GNPs into A431 SCC cells, as a function of size: (A) number of nanoparticles per single cell (significant differences were observed between all the GNP sizes, except for the comparison between 20 nm and 120 nm GNPs). (B) Total amount of gold per single cell (significant differences were observed between all the GNP sizes, except for the comparison between 50 nm and 80 nm GNPs). (C) Total surface area per single cell (significant differences were observed between all the GNP sizes). Statistical analysis was performed using one way ANOVA and Bonferroni's multiple comparison *post hoc* test, $p < 0.05$. Results presented as mean \pm SD.

the maximum number of internalized nanoparticles was obtained with 50 nm C225-GNPs. These results correlate well with previous studies, which reported that the maximum uptake of GNPs by cells, in terms of the number of nanoparticles, was observed for 50 nm nanoparticles.^{23,24}

In vivo CT experiments

Next, the ability of CT to detect tumors as a result of differently sized GNP accumulation at the tumor site was evaluated. Mice, bearing human head and neck tumors derived from the A431 SCC cell line, were systemically injected with C225-GNPs (20 nm, 50 nm, 80 nm or 120 nm); CT scans were performed prior to injection and at several time points (3 h, 6 h, 9 h and 24 h) thereafter. The results showed a clear effect of nanoparticle size on the imaging capability, with the best results obtained for 50 nm C225-GNPs. This GNP size demonstrates high-density accumulation in a tumor that is currently undetectable by anatomical CT, and yields highly distinguishable contrast enhancement. The best tumor visualization for all nanoparticle sizes was obtained 24 h post-injection, excluding 120 nm C225-GNPs, which showed very poor accumulation at the tumor site at all time points. Fig. 6 presents two-dimensional (2D) and three-dimensional (3D) CT images of a representative mouse pre-injection, in comparison with 24 h post-injection of each GNP size.

Interestingly, in mice treated with 20 nm C225-GNPs, the central region of the tumor exhibited a uniform dispersion of gold, while a relatively high amount of gold was observed in the peripheral regions, yielding a delineation of tumor boundaries. However, in mice treated with 50 nm C225-GNPs a high accumulation was exhibited mainly in the central regions, in a non-uniform manner (Fig. 7). Based on studies in cancer biology, this difference could be attributed to the different biological routes and uptake mechanisms; it is well known that the size of the nanoparticle affects its ability to overcome biological barriers and determines the rate, quantity and mechanism of cell uptake.²² We hypothesize that while 20 nm GNPs probably reach the tumor *via* the EPR effect, 50 nm GNPs are most likely taken up by detrimental macrophages that infiltrate

the tumor stroma (called tumor-associated macrophages⁴⁵), creating high-density gold clusters.

Contrast enhancement at the tumor site over time was further quantified by region-of-interest (ROI) analysis (Fig. 8). As a measure of the CT intensity, the percentage of gold voxels (voxels with high differential density) within the tumor was calculated. The minimum threshold for determining a voxel to be a gold voxel was chosen according to its grayscale index, which was defined to be higher than grayscale indices within the tumor prior to GNP injection. For 120 nm C225-GNPs, the percentage of gold voxels was close to zero at all time points. For 80 nm and 20 nm C225-GNPs, this value slightly increased until 24 h, whereas after 24 h 20 nm C225-GNPs demonstrated a value over 3 times higher than 80 nm GNPs. Interestingly, with 50 nm C225-GNPs, a significant enhancement in the CT intensity was observed as early as 3 h post-injection, remaining high compared to all other GNP sizes at all the time points examined, and reaching an enhancement at 24 h post-injection, over 5 times higher than 20 nm C225-GNPs (Fig. 8A and B).

Due to the significant advantage of 50 nm C225-GNPs over the other sizes, we further examined contrast enhancement by performing additional scans, up to 48 h post-injection, in mice treated with this GNP size. As shown in Fig. 9, after 24 h no further increase was observed in contrast enhancement, but rather a minor decrease, suggesting this time point as optimal for imaging.

Biodistribution of GNPs

Next, the pharmacokinetics, the whole-body biodistribution, and the degree of tumor uptake of the GNPs of various sizes 24 h post-injection were examined, using FAAS to quantitatively measure gold concentrations in the tumor and various organs (Fig. 10A). The 50 nm, 80 nm and 120 nm C225-GNPs were found to undergo full clearance from the bloodstream after 24 h, while 20 nm C225-GNPs demonstrated an extended blood circulation time. Nanoparticles accumulated in the spleen, kidneys, and liver, corresponding to their well-described clearance mechanism.^{46,47} Tumor uptake was strongly affected by the nanoparticle size: unlike CT analysis results, but consistent with previous studies showing an inverse

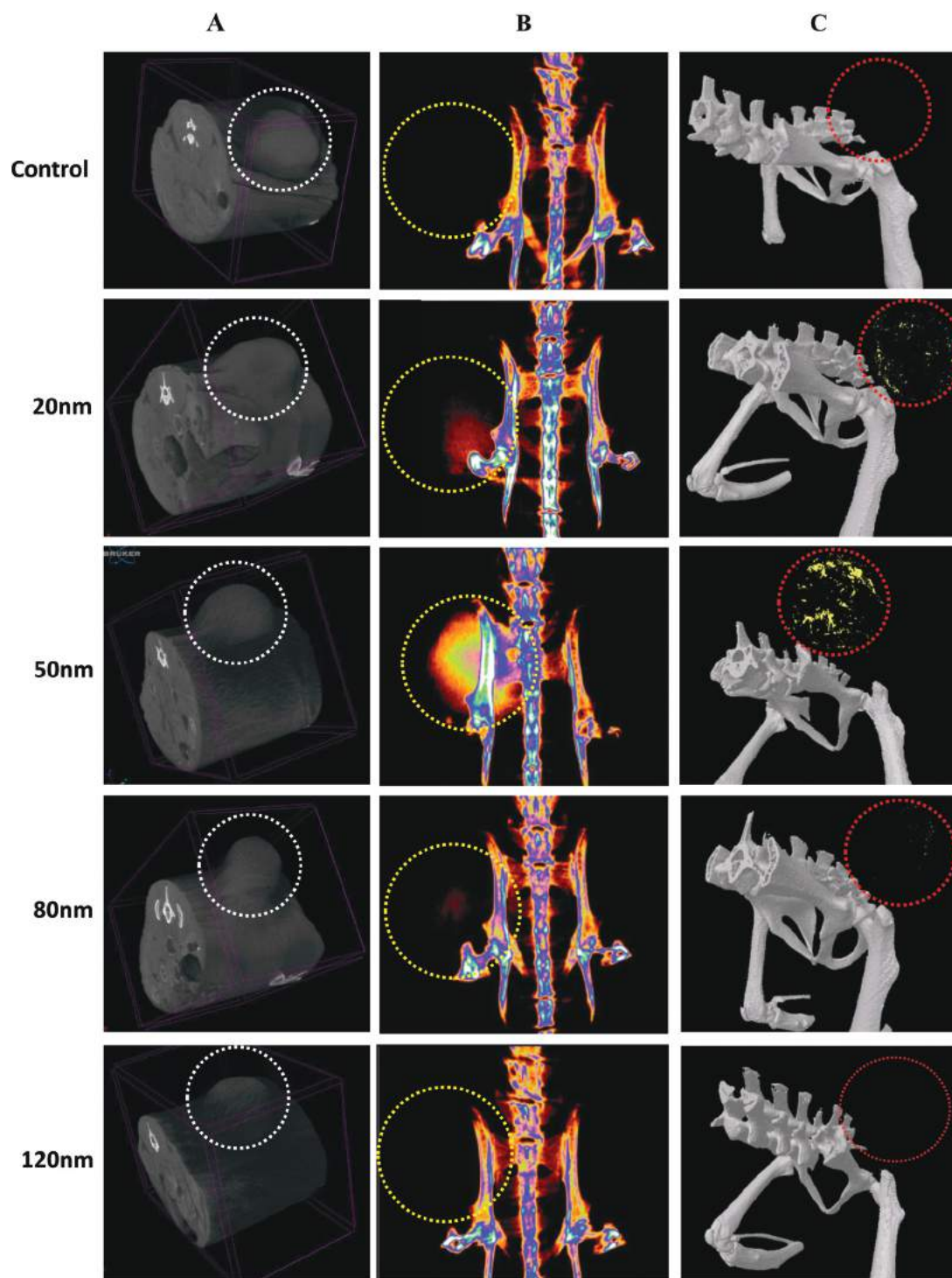


Fig. 6 CT images of a representative mouse pre-injection (control) and 24 h post-injection of 20 nm, 50 nm, 80 nm, and 120 nm C225-GNPs. (A) Surface rendered images; (B) maximum intensity projection 2D images; (C) volume rendered 3D images. Circles indicate tumor sites; GNP accumulation leads to contrast enhancement in tumors which are currently undetectable by anatomical CT. The highest enhancement was obtained for 50 nm C225-GNPs.

correlation between nanoparticle size and tumor uptake,^{29,30} the maximum tumor uptake was observed after injection of 20 nm C225-GNPs with an Au concentration of 0.3 mg per g-tissue (which is 5% of the injected dose (ID) per g tissue).

Larger GNP sizes led to lower tumor uptake, with zero gold concentration in tumors of mice treated with 120 nm C225-GNPs. This trend was maintained when the internalized Au mass was translated into number of GNPs, total gold volume and total

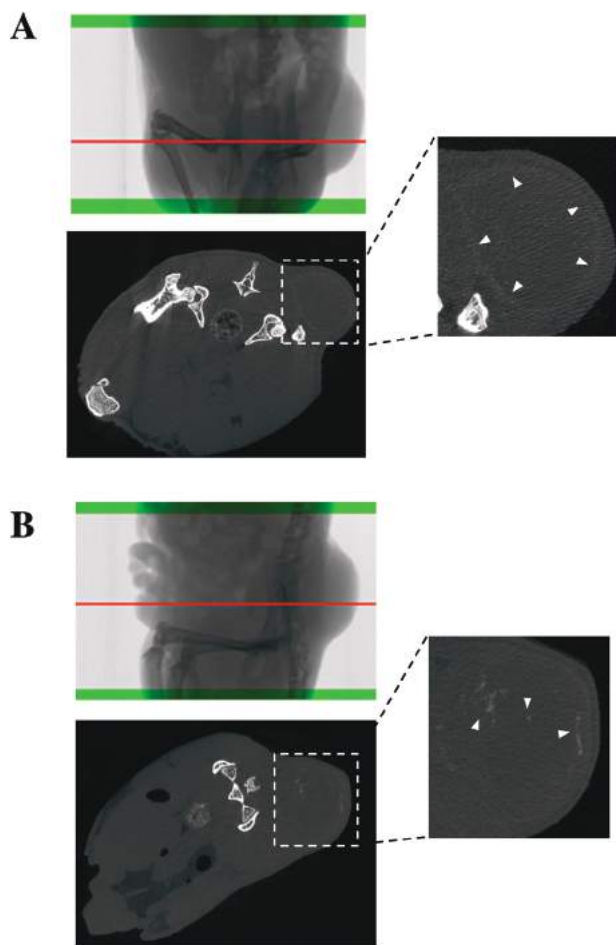


Fig. 7 Axial CT images of the tumor area 24 h post-injection of: (A) 20 nm C225-GNPs; and (B) 50 nm C225-GNPs. 20 nm C225-GNPs demonstrated delineation of tumor boundaries, while 50 nm C225-GNPs exhibited high-density gold clusters in the tumor central region.

surface area (Fig. 10B). Differences were more significant in the total surface area than in the total gold volume, suggesting that for drug-encapsulated nanoparticles, and especially for drug-

coated nanoparticles, a smaller nanoparticle size has higher potential in drug delivery.

An important phenomenon presented here is the non-correlation between *in vitro* and *in vivo* results. While the *in vitro* experiments showed low cellular uptake for 20 nm GNPs, and high cellular uptake for 120 nm GNPs, the *in vivo* experiments, which are far more complex than *in vitro* models and simulate a more biologically relevant system, demonstrated virtually contradictory conclusions. Thus, despite the great importance of preliminary *in vitro* studies when investigating processes at the cellular level, such studies have limited predictability for living systems.

In addition, our results further demonstrate a partial discrepancy between the total amount of gold accumulated in the tumor and the resultant CT contrast. The highest amount of gold accumulated in the tumor was obtained with the smallest 20 nm C225-GNPs, while the highest CT contrast enhancement in the tumor was obtained with the 50 nm C225-GNPs. This disparity may arise from the different distribution patterns of differently sized GNPs. In CT, the distribution pattern of GNPs within the tumor has opposite implications on two inter-related parameters, which influence tumor visualization: the number of voxels containing gold and the total amount of gold per voxel. Though the first parameter increases with higher distribution, the second parameter rather decreases. Thus, a high dispersion of gold may result in many low-density voxels which can sometimes go undetected by CT. However, accumulation of gold in limited areas leads to high density voxels which can easily be detected by CT. Therefore, although 50 nm C225-GNPs are taken into the tumor to a lesser extent than 20 nm C225-GNPs, they yield a stronger differential signal in CT due to their non-uniform dispersion in the central region of the tumor and their tendency to build clusters of high gold concentrations. Thus, we suggest that for this model, as well as similar cancer models characterized by the same aggressiveness level and the same vascular permeability, 50 nm GNPs are better candidates for tumor imaging despite their lower potential for drug delivery.

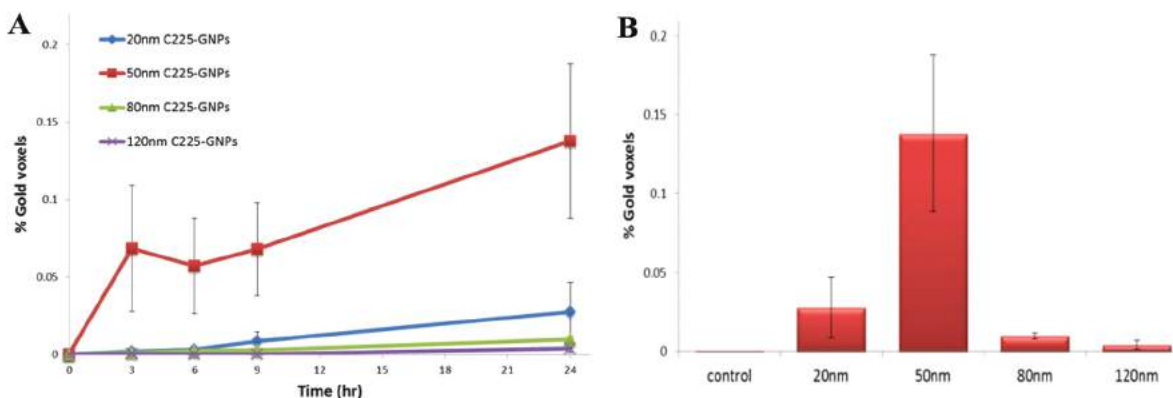


Fig. 8 ROI analysis: contrast enhancement in tumors after injection of 20 nm, 50 nm, 80 nm and 120 nm C225-GNPs. (A) Measurements over time; (B) focus on 24 h post-injection: 50 nm C225-GNPs exhibit significantly higher contrast enhancement in comparison with each one of the other GNP sizes (one way ANOVA and Bonferroni's multiple comparison *post hoc* test, $p < 0.05$). Results presented as mean \pm SD.

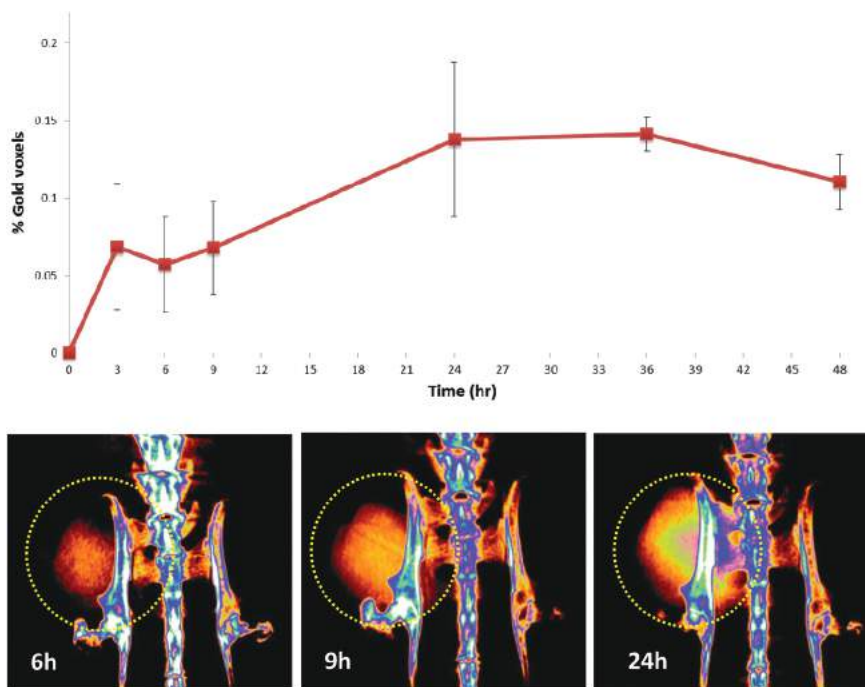


Fig. 9 Top: ROI analysis: contrast enhancement in the tumor, up to 48 h post-injection of 50 nm C225-GNPs. A minor decrease was observed from 36 h to 48 h post-injection. Results presented as mean \pm SD. Bottom: maximum intensity projection images of a representative mouse 6 h, 9 h and 24 h after injection of 50 nm C225-GNPs.

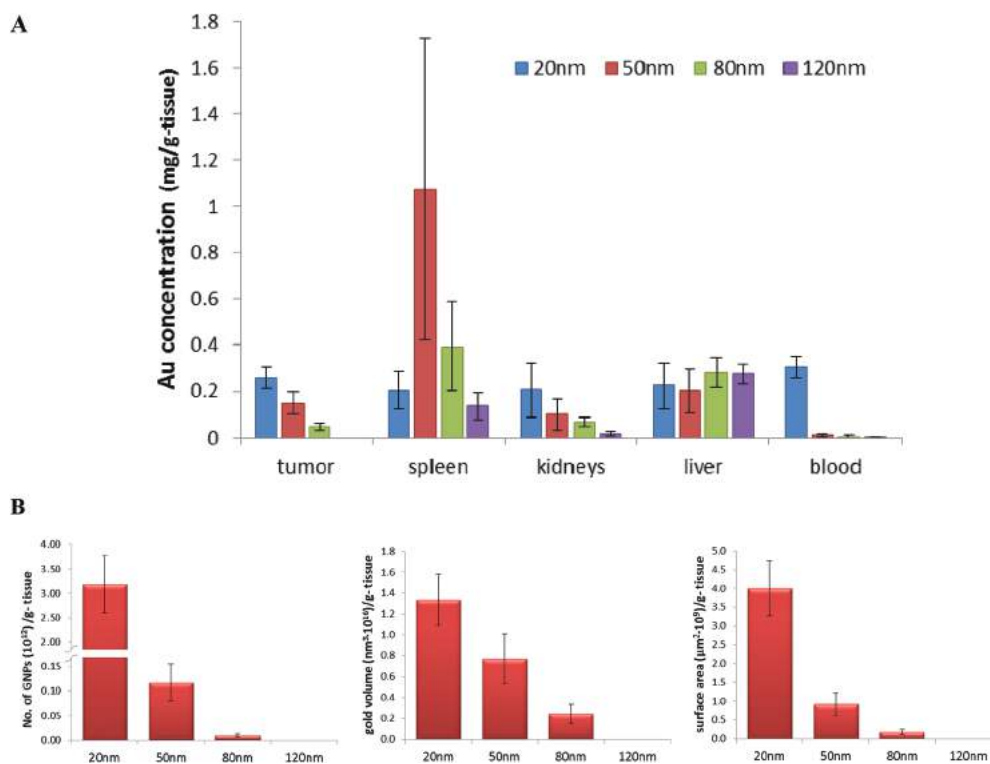


Fig. 10 Biodistribution of the size series of C225-GNPs in mice: (A) gold concentrations in the tumor and main organs 24 h post injection, as quantitatively measured by FAAS. Gold concentration in the blood after injection of 20 nm C225-GNPs was significantly higher than after injection of the other sizes ($p < 0.01$). In the tumor, significant differences were observed between 20 nm and 80 nm C225-GNPs ($p < 0.05$) and between 20 nm and 120 nm C225-GNPs ($p < 0.01$). (B) Focus on tumor uptake: translation to the number of GNPs, total gold volume and total surface area per g tissue. Significant difference was observed between 20 nm and 50 nm C225-GNPs ($p < 0.05$) in terms of the number of GNPs and the total surface area. Statistical analysis was performed using one way ANOVA and Bonferroni's multiple comparison *post hoc* test. Values presented as mean \pm SD.

Conclusions

In the present study, we examined the effect of the size of anti-EGFR-coated GNPs on tumor uptake and tumor visualization by CT. We performed *in vitro* and *in vivo* experiments, showing a strong dependence on the size of the GNP for both drug delivery strategies (tumor uptake) and tumor imaging (differential contrast enhancement). It is important to note that though this study did not examine directly the particle's therapeutic abilities, there is a clear correlation between the degree of tumor uptake and drug delivery capabilities. Interestingly, we found a partial discrepancy between the total amount of gold accumulated in the tumor, and the capability of the GNP to produce imaging contrast. The highest amount of gold accumulated within the tumor was obtained with the smallest 20 nm C225-GNPs, while the highest CT contrast enhancement in the tumor was obtained with 50 nm C225-GNPs. This disparity may stem from the different distribution patterns of differently sized GNPs in the tumor. 20 nm C225-GNPs exhibited a high dispersion in the tumor, yielding many low density, undistinguishable voxels, while 50 nm C225-GNPs tended to build clusters of high gold concentrations, yielding a strong differential signal in CT.

This study further demonstrates the limited predictability of *in vitro* nanoparticle uptake studies for complex living systems. While the *in vitro* experiments showed low cellular uptake for 20 nm GNPs, and high cellular uptake for 120 nm GNPs, the *in vivo* experiments, which are far more complex and simulate a more biologically relevant system, demonstrated virtually opposite conclusions. Thus, despite the great importance of preliminary *in vitro* studies when investigating processes at the cellular level, such studies have limited predictability for living systems.

The results also suggest that in general, the optimal particle for therapy, which should show maximum uptake into the diseased tissue, is not always optimal for tissue imaging. Therefore, an alternative route to the one-size-fits-all approach, in which a mixture consists of an optimized ratio between differently sized nanoparticles, should be considered for theranostic applications. Our results better correlate nanoparticle properties with their biological effects and highlight the tremendous consequences of nanoparticle design on its activity *in vivo*. This issue should be further investigated in other imaging modalities that use nanoparticle-based contrast agents. Moreover, our findings are meaningful for future research in the fields of molecular imaging and nanomedicine, and pose a challenge for designing optimal nanoparticles for theranostic applications.

Conflict of interest disclosure

The authors have declared that no competing interest exists.

Acknowledgements

This work was partially supported by the Israel Cancer Research Fund (ICRF), by the Israel Science Foundation (grant # 749/14) and by the Christians for Israel Chair in Medical Research.

References

- 1 J. Harrell and R. Kopelman, Biocompatible probes measure intracellular activity, *Biophotonics Int.*, 2000, 7, 22–24.
- 2 J. Funkhouser, Reinventing pharma: The theranostic revolution, *Curr. Drug Discovery Technol.*, 2002, 2, 17–19.
- 3 M. A. Hahn, A. K. Singh, P. Sharma, S. C. Brown and B. M. Moudgil, Nanoparticles as contrast agents for in-vivo bioimaging: current status and future perspectives, *Anal. Bioanal. Chem.*, 2011, 399, 3–27.
- 4 K. Cho, X. Wang, S. Nie and D. M. Shin, Therapeutic nanoparticles for drug delivery in cancer, *Clin. Cancer Res.*, 2008, 14, 1310–1316.
- 5 R. A. Petros and J. M. DeSimone, Strategies in the design of nanoparticles for therapeutic applications, *Nat. Rev. Drug Discovery*, 2010, 9, 615–627.
- 6 S. S. Kelkar and T. M. Reineke, Theranostics: combining imaging and therapy, *Bioconjugate Chem.*, 2011, 22, 1879–1903.
- 7 H. Maeda, The enhanced permeability and retention (EPR) effect in tumor vasculature: the key role of tumor-selective macromolecular drug targeting, *Adv. Enzyme Regul.*, 2001, 41, 189–207.
- 8 H. Maeda, J. Wu, T. Sawa, Y. Matsumura and K. Hori, Tumor vascular permeability and the EPR effect in macromolecular therapeutics: a review, *J. Controlled Release*, 2000, 65, 271–284.
- 9 K. Y. Choi, G. Liu, S. Lee and X. Chen, Theranostic nano-platforms for simultaneous cancer imaging and therapy: current approaches and future perspectives, *Nanoscale*, 2012, 4, 330–342.
- 10 Q. Quan, *et al.*, HSA coated iron oxide nanoparticles as drug delivery vehicles for cancer therapy, *Mol. Pharm.*, 2011, 8, 1669–1676.
- 11 Z. Medarova, W. Pham, C. Farrar, V. Petkova and A. Moore, In vivo imaging of siRNA delivery and silencing in tumors, *Nat. Med.*, 2007, 13, 372–377.
- 12 J. T. Robinson, *et al.*, High performance in vivo near-IR (>1 μm) imaging and photothermal cancer therapy with carbon nanotubes, *Nano Res.*, 2010, 3, 779–793.
- 13 A. M. Gobin, *et al.*, Near-infrared resonant nanoshells for combined optical imaging and photothermal cancer therapy, *Nano Lett.*, 2007, 7, 1929–1934.
- 14 J. Kim, *et al.*, Designed fabrication of multifunctional magnetic gold nanoshells and their application to magnetic resonance imaging and photothermal therapy, *Angew. Chem., Int. Ed.*, 2006, 118, 7918–7922.

- 15 X. Huang, I. H. El-Sayed, W. Qian and M. A. El-Sayed, Cancer cell imaging and photothermal therapy in the near-infrared region by using gold nanorods, *J. Am. Chem. Soc.*, 2006, **128**, 2115–2120.
- 16 K. Kim, *et al.*, Tumor-homing multifunctional nanoparticles for cancer theragnosis: simultaneous diagnosis, drug delivery, and therapeutic monitoring, *J. Controlled Release*, 2010, **146**, 219–227.
- 17 N. Rapoport, Z. Gao and A. Kennedy, Multifunctional nanoparticles for combining ultrasonic tumor imaging and targeted chemotherapy, *J. Natl. Cancer Inst.*, 2007, **99**, 1095–1106.
- 18 C. E. Ashley, *et al.*, The targeted delivery of multicomponent cargos to cancer cells by nanoporous particle-supported lipid bilayers, *Nat. Mater.*, 2011, **10**, 389–397.
- 19 K. Jakobsohn, M. Motiei, M. Sinvani and R. Popovtzer, Towards real-time detection of tumor margins using photothermal imaging of immune-targeted gold nanoparticles, *Int. J. Nanomedicine*, 2012, **7**, 4707.
- 20 R. Ankri, *et al.*, Intercoupling surface plasmon resonance and diffusion reflection measurements for real-time cancer detection, *J. Biophotonics*, 2013, **6**, 188–196.
- 21 O. Betzer, *et al.*, Nanoparticle-based CT imaging technique for longitudinal and quantitative stem cell tracking within the brain: application in neuropsychiatric disorders, *ACS Nano*, 2014, **8**, 9274–9285.
- 22 A. Albanese, P. S. Tang and W. C. Chan, The effect of nanoparticle size, shape, and surface chemistry on biological systems, *Annu. Rev. Biomed. Eng.*, 2012, **14**, 1–16.
- 23 B. D. Chithrani, A. A. Ghazani and W. C. Chan, Determining the size and shape dependence of gold nanoparticle uptake into mammalian cells, *Nano Lett.*, 2006, **6**, 662–668.
- 24 A. Malugin and H. Ghandehari, Cellular uptake and toxicity of gold nanoparticles in prostate cancer cells: a comparative study of rods and spheres, *J. Appl. Toxicol.*, 2010, **30**, 212–217.
- 25 S. Hirn, *et al.*, Particle size-dependent and surface charge-dependent biodistribution of gold nanoparticles after intravenous administration, *Eur. J. Pharm. Biopharm.*, 2011, **77**, 407–416.
- 26 G. Sonavane, K. Tomoda and K. Makino, Biodistribution of colloidal gold nanoparticles after intravenous administration: effect of particle size, *Colloids Surf., B*, 2008, **66**, 274–280.
- 27 W. H. De Jong, *et al.*, Particle size-dependent organ distribution of gold nanoparticles after intravenous administration, *Biomaterials*, 2008, **29**, 1912–1919.
- 28 W.-S. Cho, *et al.*, Size-dependent tissue kinetics of PEG-coated gold nanoparticles, *Toxicol. Appl. Pharmacol.*, 2010, **245**, 116–123.
- 29 K. Huang, *et al.*, Size-dependent localization and penetration of ultrasmall gold nanoparticles in cancer cells, multicellular spheroids, and tumors in vivo, *ACS Nano*, 2012, **6**, 4483–4493.
- 30 G. Zhang, *et al.*, Influence of anchoring ligands and particle size on the colloidal stability and in vivo biodistribution of polyethylene glycol-coated gold nanoparticles in tumor-xenografted mice, *Biomaterials*, 2009, **30**, 1928–1936.
- 31 S. D. Perrault, C. Walkey, T. Jennings, H. C. Fischer and W. C. Chan, Mediating tumor targeting efficiency of nanoparticles through design, *Nano Lett.*, 2009, **9**, 1909–1915.
- 32 Z. Yang, *et al.*, Pharmacokinetics and biodistribution of near-infrared fluorescence polymeric nanoparticles, *Nanotechnology*, 2009, **20**, 165101.
- 33 T. Reuveni, M. Motiei, Z. Romman, A. Popovtzer and R. Popovtzer, Targeted gold nanoparticles enable molecular CT imaging of cancer: an in vivo study, *Int. J. Nanomedicine*, 2011, **6**, 2859.
- 34 R. Duncan, Polymer conjugates for tumour targeting and intracytoplasmic delivery. The EPR effect as a common gateway?, *Pharm. Sci. Technol. Today*, 1999, **2**, 441–449.
- 35 H. Haigler, J. Ash, S. Singer and S. Cohen, Visualization by fluorescence of the binding and internalization of epidermal growth factor in human carcinoma cells A-431, *Proc. Natl. Acad. Sci. U. S. A.*, 1978, **75**, 3317–3321.
- 36 J. R. Grandis, *et al.*, Levels of TGF- α and EGFR protein in head and neck squamous cell carcinoma and patient survival, *J. Natl. Cancer Inst.*, 1998, **90**, 824–832.
- 37 B. Enustun and J. Turkevich, Coagulation of colloidal gold, *J. Am. Chem. Soc.*, 1963, **85**, 3317–3328.
- 38 S. M. Moghimi, A. C. Hunter and J. C. Murray, Long-circulating and target-specific nanoparticles: theory to practice, *Pharmacol. Rev.*, 2001, **53**, 283–318.
- 39 A. Abuchowski, T. Van Es, N. Palczuk and F. Davis, Alteration of immunological properties of bovine serum albumin by covalent attachment of polyethylene glycol, *J. Biol. Chem.*, 1977, **252**, 3578–3581.
- 40 X. Qian, *et al.*, In vivo tumor targeting and spectroscopic detection with surface-enhanced Raman nanoparticle tags, *Nat. Biotechnol.*, 2008, **26**, 83–90.
- 41 L. Feldkamp, L. Davis and J. Kress, Practical cone-beam algorithm, *JOSA A*, 1984, **1**, 612–619.
- 42 G. Yan, J. Tian, S. Zhu, Y. Dai and C. Qin, Fast cone-beam CT image reconstruction using GPU hardware, *J. X-ray Sci. Technol.*, 2008, **16**, 225–234.
- 43 L. A. Austin, B. Kang, C.-W. Yen and M. A. El-Sayed, Nuclear targeted silver nanospheres perturb the cancer cell cycle differently than those of nanogold, *Bioconjugate Chem.*, 2011, **22**, 2324–2331.
- 44 T. A. Larson, J. Bankson, J. Aaron and K. Sokolov, Hybrid plasmonic magnetic nanoparticles as molecular specific agents for MRI/optical imaging and photothermal therapy of cancer cells, *Nanotechnology*, 2007, **18**, 325101.
- 45 R. Weissleder, M. Nahrendorf and M. J. Pittet, Imaging macrophages with nanoparticles, *Nat. Mater.*, 2014, **13**, 125–138.
- 46 S.-D. Li and L. Huang, Pharmacokinetics and biodistribution of nanoparticles, *Mol. Pharm.*, 2008, **5**, 496–504.
- 47 J. P. M. Almeida, A. L. Chen, A. Foster and R. Drezek, In vivo biodistribution of nanoparticles, *Nanomedicine*, 2011, **6**, 815–835.